Mon. Not. R. Astron. Soc. **000**, 1–11 (2010) Printed 18 October 2013 (MN LATEX style file v2.2)

X-ray emission from star-forming galaxies - III. Calibration of the $L_{\rm X} - {\rm SFR}$ relation up to redshift $z \approx 1.3$

S. Mineo[1,2,3⋆], M. Gilfanov [2,4], B. D. Lehmer[5,6], G. E. Morrison[7,8] and R. Sunyaev [2,4]
[1] *Harvard-Smithsonian Center for Astrophysics, 60 Garden Street Cambridge, MA 02138, USA*
[2] *Max Planck Institut für Astrophysik, Karl-Schwarzschild-Str. 1 85741 Garching, Germany*
[3] *Department of Physics, University of Durham, South Road, Durham DH1 3LE, UK*
[4] *Space Research Institute of Russian Academy of Sciences, Profsoyuznaya 84/32, 117997 Moscow, Russia*
[5] *The Johns Hopkins University, Homewood Campus, Baltimore, MD 21218, USA*
[6] *NASA Goddard Space Flight Centre, Code 662, Greenbelt, MD 20771, USA*
[7] *Institute for Astronomy, University of Hawaii, Manoa, HI 96822, USA*
[8] *Canada France Hawaii Telescope Corp., Kamuela, HI 96743, USA*

Accepted. Received; in original form

ABSTRACT

We investigate the relation between total X-ray emission from star-forming galaxies and their star formation activity. Using nearby late-type galaxies and ULIRGs from Paper I and star-forming galaxies from *Chandra* Deep Fields, we construct a sample of 66 galaxies spanning the redshift range $z \approx 0 - 1.3$ and the star-formation rate (SFR) range $\sim 0.1 - 10^3\,M_{\odot}\,{\rm yr}^{-1}$. In agreement with previous results, we find that the $L_{\rm X} - {\rm SFR}$ relation is consistent with a linear law both at $z = 0$ and for the $z = 0.1 - 1.3$ CDF galaxies, within the statistical accuracy of ~ 0.1 in the slope of the $L_{\rm X} - {\rm SFR}$ relation. For the total sample, we find a linear scaling relation $L_{\rm X}/{\rm SFR} \approx (4.0 \pm 0.4) \times 10^{39} ({\rm erg\,s^{-1}})/(M_{\odot}\,{\rm yr}^{-1})$, with a scatter of ≈ 0.4 dex. About $\sim 2/3$ of the 0.5–8 keV luminosity generated per unit SFR is expected to be due to HMXBs. We find no statistically significant trends in the mean $L_{\rm X}/{\rm SFR}$ ratio with the redshift or star formation rate and constrain the amplitude of its variations by $\lesssim 0.1 - 0.2$ dex. These properties make X-ray observations a powerful tool to measure the star formation rate in normal star-forming galaxies that dominate the source counts at faint fluxes.

Key words: X-rays: galaxies – galaxies: star formation – galaxies: starburst – X-rays: ISM – X-rays: binaries.

1 INTRODUCTION

High-mass X-ray binaries (HMXBs) and the hot ionized inter-stellar medium (ISM) are the main contributors to the total X-ray output of normal (i.e. not containing a luminous active galactic nucleus (AGN)) star-forming galaxies. It is well established that the collective X-ray luminosity of HMXBs well correlates with the star formation activity of the host galaxy (Grimm, Gilfanov, & Sunyaev 2003; Ranalli, Comastri, & Setti 2003; Lehmer et al. 2010; Mineo, Gilfanov, & Sunyaev 2011, 2012, hereafter Paper I). The hot ionized ISM contributes about $\sim 1/4$ to the observed X-ray emission from late-type galaxies in the standard X-ray band (0.5–8 keV), its luminosity has been also shown to scale linearly with star formation rate (SFR) (Grimes et al. 2005; Li & Wang 2012; Mineo, Gilfanov, & Sunyaev 2012, hereafter Paper II). Thus, it has been proposed that the total, integrated X-ray luminosity from star-forming galaxies can be used as a proxy of the SFR (Grimm, Gilfanov, & Sunyaev 2003; Ranalli, Comastri, & Setti 2003). Although not entirely free from its own systematic uncertainties and contaminations, the X-ray based SFR proxy is less affected by the interstellar extinction and cosmological passband redshift, than conventional SFR indicators. Furthermore, the $L_{\rm X} - {\rm SFR}$ scaling relation does not experience significant cosmological evolution up to redshifts of $z \sim 1 - 2$. This has been initially suggested based on direct measurements of the $L_{\rm X}/{\rm SFR}$ ratios for several galaxies in Chandra Deep Fields (Grimm, Gilfanov, & Sunyaev 2003; Lehmer et al. 2008, 2010; Mineo, Gilfanov, & Sunyaev 2012) and was further supported by calculations of the maximal contribution of X-ray faint star-forming galaxies to the unresolved part of the Cosmic X-ray background (Dijkstra et al. 2012) and

⋆ E-mail: smineo@head.cfa.harvard.edu

stacking analysis results (Cowie, Barger, & Hasinger 2012). These properties make the X-ray based SFR proxy a powerful tool to measure the star formation rate in distant galaxies.

The most significant systematic effect which can compromise the X-ray-based SFR measurements is the contamination by the emission of the central supermassive black hole, the AGN. Indeed, even low luminosity AGN, with $\log(L_{\rm X}) \sim 42$ can outshine a $\sim 100 M_{\odot}$/yr starburst. As populations of bright galaxies are mainly composed of AGN (for recent results, see e.g. Xue et al. 2011; Lehmer et al. 2012), SFR measurements using X-ray luminosity can be applied only to a relatively small fraction of bright galaxies. In this case, a careful investigation of the nature of each galaxy is required in order to separate late-type from early-type galaxy populations. On the contrary, among faint sources, $F_{\rm X} \lesssim 10^{-17}$ erg cm^{-2} s^{-1}, the majority are star-forming galaxies located at moderate and large redshifts, $z \sim 0.5-3$ (Cowie, Barger, & Hasinger 2012; Lehmer et al. 2012). This makes the X-ray based SFR proxy a powerful tool to measure the star formation rate in faint galaxies, where it can be used *en masse*, to infer the cosmic star formation history (e.g. Cowie, Barger, & Hasinger 2012).

The aim of this paper is to obtain the $L_{\rm X}-$SFR scaling relation for the *total* X-ray luminosity and to investigate its behavior in a broad range of redshifts. For the redshift $z = 0$, we use the sample of star-forming galaxies and ULIRGs (ultra-luminous infrared galaxies) from Papers I and II. We then select normal star-forming galaxies from the *Chandra* Deep Fields (CDFs) expanding the local sample towards cosmologically interesting redshifts and high star formation rates. We combine these data in order to calibrate the $L_{\rm X}-$SFR scaling relation over a broad range of redshifts and star formation rates.

The structure of the paper is as follows. In Section 2 we briefly summarize the selection criteria and properties of the local sample. In Section 3 we describe selection of late-type galaxies from the CDF data and the procedures used to calculate their X-ray luminosities and star formation rates. The $L_{\rm X}-$SFR relation is derived in Section 4 and its redshift and SFR dependences are investigated in Section 5. In Section 6 we summarize our findings.

Throughout this paper we assume a flat ΛCDM cosmology with $H_0 = 70$ km/s/Mpc, $\Omega_M = 0.3$ and $\Omega_\Lambda = 0.7$.

2 LOCAL GALAXIES

2.1 The sample

We constructed the local sample of star-forming galaxies by merging a sample of nearby galaxies resolved by *Chandra* from Paper II (Sect. 2, Table 1), and a sample of unresolved LIRGs (luminous infrared galaxies) and ULIRGs defined in Paper I (Sect. 2.2, Table 2). The local sample contains 29 star-forming galaxies, their parameters are summarized in Table 1.

The SFRs and stellar masses ($M_\star$) were determined in Paper I, based on far-infrared, UV and K-band luminosities. These quantities were measured for the same spatial regions as used for computing the X-ray luminosities, defined in Section 5 of Paper I. The star formation rates and stellar masses of the local sample span broad ranges, from $\sim 0.1-290\,M_{\odot}\,{\rm yr}^{-1}$ and $\sim 3\times10^{8}-2\times10^{11}\,M_{\odot}$, respectively.

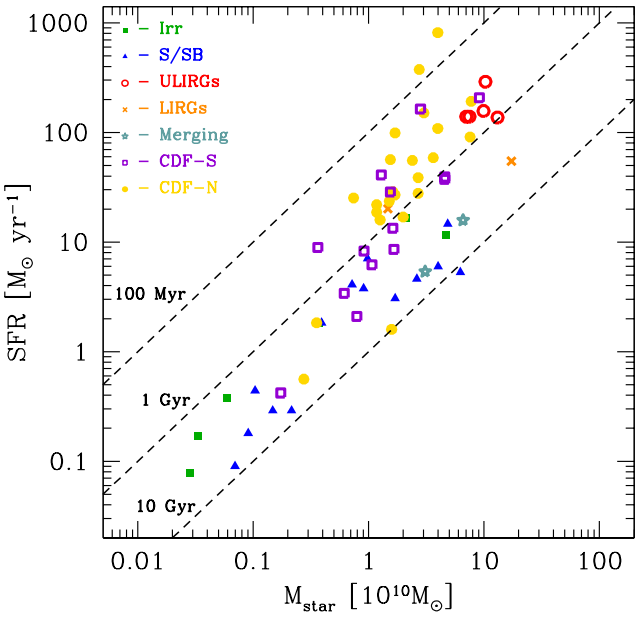

Figure 1. The SFR $- M_\star$ plane. Different types of galaxies are plotted with different symbols: Irregulars in (green) filled squares, spirals in (blue) filled triangles, ULIRGs in (red) empty circles, LIRGs in (orange) crosses, interacting systems in (cyan) empty stars. Star-forming galaxies from CDF-S and CDF-N are plotted as empty squares (purple) and filled circles (gold) respectively. The dashed lines correspond to constant stellar-mass-to-SFR ratio.

2.2 Total X-ray luminosity

The data preparation was done following standard CIAO[1] threads (CIAO version 3.4; CALDB version 3.4.1), exactly the same way as described in Sect. 3 of Paper I.

For resolved galaxies, listed in the first part of Table 1, source spectra were extracted in the 0.5–8 keV energy band and background spectra were created as described in Sect. 3.3 of Paper II. Spatial regions for extracting source spectra were defined in Paper I. Both source and background spectra and the associated ARF and RMF files were produced by using `specextract` script and modeled using XSPEC v. 12.3.1x. The spectra were grouped in order to have a minimum of 15 counts per channel to apply the χ^2 fitting. For most of the spectra a good fit was obtained with a two component model: a thermal plasma (`mekal`) plus a power-law, corrected for the Galactic absorption. A second photoelectric absorption component, accounting for the intrinsic absorption and/or a second thermal component, was required for some of the galaxies. The addition of such a component was decided on a galaxy-by-galaxy basis via the result of the F-test, using a probability of 10^{-3} as the threshold (see Paper II for details). For each galaxy, we used the best fit model to calculate the count-to-erg conversion coefficient.

[1] http://cxc.harvard.edu/ciao3.4/index.html

Table 1. The local ($z = 0$) sample of star-forming galaxies.

Galaxy	D (Mpc)	Ref.[a]	Hubble type	SFR[b] ($M_\odot\,\mathrm{yr}^{-1}$)	$M_\star$[c] ($10^{10}\,M_\odot$)	$\log L_\mathrm{X}^\mathrm{tot}$[d] ($\mathrm{erg\,s}^{-1}$)
RESOLVED GALAXIES						
NGC 0278	$11.8^{+2.4}_{-2.0}$	(2)	SAB(rs)b	4.1	0.7	39.52
NGC 0520	$27.8^{+5.6}_{-4.7}$	(2)	Pec	11.6	4.7	40.53
NGC 1313	4.1 ± 0.2	(3)	SB(s)d	0.44	0.1	39.75
NGC 1569	1.9 ± 0.2	(4)	IB	7.8×10^{-2}	2.8×10^{-2}	38.17
NGC 2139	$26.7^{+5.8}_{-4.8}$	(5)	SAB(rs)cd	3.8	0.91	40.48
NGC 3079	18.2	(1)	SB(s)c	6.0	4.0	40.30
NGC 3310	19.8	(1)	SAB(r)bc pec	7.1	0.98	41.02
NGC 3556	$10.7^{+1.9}_{-1.6}$	(11)	SB(s)cd	3.1	1.7	39.87
NGC 3631	24.3 ± 1.6	(7)	SA(s)c	4.6	2.6	40.79
NGC 4038/39	13.8 ± 1.7	(8)	-	5.4	3.1	40.57
NGC 4194	$39.1^{+7.9}_{-6.6}$	(2)	IBm pec	16.8	2.1	40.92
NGC 4214	2.5 ± 0.3	(9)	IAB(s)m	0.17	3.3×10^{-2}	38.53
NGC 4490	$7.8^{+1.6}_{-1.3}$	(2)	SB(s)d pec	1.8	0.39	40.32
NGC 4625	$8.2^{+1.7}_{-1.4}$	(2)	SAB(rs)m pec	0.09	7.0×10^{-2}	37.92
NGC 5253	4.1 ± 0.5	(6)	Im pec	0.38	5.9×10^{-2}	38.31
NGC 5474	6.8	(10)	SA(s)cd pec	0.18	9.1×10^{-2}	39.05
NGC 5775	$26.7^{+11.9}_{-8.2}$	(2)	Sb(f)	5.3	6.3	40.88
NGC 7090	7.6	(1)	SBc	0.29	0.22	39.08
NGC 7541	$34.9^{+6.6}_{-5.7}$	(5)	SB(rs)bc pec	14.7	4.9	40.39
NGC 7793	$4.0^{+0.7}_{-0.6}$	(11)	SA(s)d	0.29	0.15	38.53
UGC 05720	$24.9^{+11.1}_{-7.7}$	(2)	Im pec	1.8	0.37	39.77
UNRESOLVED GALAXIES						
IRAS 17208-0014	183.0	(1)	ULIRG	289.9	10.3	41.40
IRAS 20551-4250	179.1	(1)	ULIRG	139.4	7.5	41.63
IRAS 23128-5919	184.2	(1)	ULIRG	139.6	7.0	41.88
IRAS 10565+2448	182.6	(1)	ULIRG	156.8	9.9	41.42
IRAS 13362+4831	120.9	(1)	LIRG	54.8	17.3	41.81
IRAS 09320+6134	164.3	(1)	ULIRG	137.1	13.1	41.39
IRAS 00344-3349	84.0	(1)	LIRG	20.1	1.5	41.23
NGC 4676	98.2	(1)	-	15.8	6.6	40.92

[a] References for distances: (1) Sanders et al. (2003), (2) Tully (1988), (3) Grisé et al. (2008), (4) Makarova & Karachentsev (2003), (5) Willick et al. (1997), (6) Saha et al. (2006), (7) Ismail et al. (2005), (8) Saviane, Hibbard, & Rich (2004), (9) Drozdovsky et al. (2002), (10) Drozdovsky & Karachentsev (2000), (11) Tully et al. (2009).
[b] Star formation rate from Spitzer and GALEX data (see Sect. 6 Paper I).
[c] Stellar mass from 2MASS data (see Sect. 5 Paper I).
[d] Total X-ray luminosity of galaxies, i.e. gas and X-ray binary contribution, in 0.5–8 keV band, measured as described in Sect. 2.2.

Using this coefficient, the energy flux was computed form the background subtracted source count rate.

For the sample of unresolved starburst galaxies presented in the second part of Table 1, we adopted 0.5–8 keV luminosities from Paper I.

3 STAR-FORMING GALAXIES FROM CHANDRA DEEP FIELDS

In order to extend the $L_\mathrm{X} - \mathrm{SFR}$ relation towards higher redshifts and SFRs, we selected a sample of late-type galaxies in the Chandra Deep Fields. We started from the samples studied by Lehmer et al. (2008), who selected late-type galaxies in the 2 Ms Chandra Deep Field-North (CDF-N; Alexander et al. 2003) and Extended Chandra Deep Field-South (E-CDF-S; Lehmer et al. 2005), and by Xue et al. (2011), the 4 Ms Chandra Deep Field-South (CDF-S) survey. For the E-CDF-S, the Lehmer et al. (2008) late-type galaxy sample was constructed using data within a 1 Ms *Chandra* exposure of the CDF-S proper (Alexander et al. 2003) and four flanking E-CDF-S fields with 250 ksec *Chandra* exposures each (Lehmer et al. 2005). The Xue et al. (2011) 4 Ms exposure covered only the CDF-S but to ≈4–16 times larger depth.

As we describe in the sections below, to study the L_X–SFR correlation and its redshift dependence, we filtered these samples according to the following criteria: (i) rigorous determination of the morphological type appropriate for a star-forming galaxy; (ii) availability of a robust 0.5–8

Table 2. Late-type galaxies from the *Chandra* Deep Fields.

CXO	Redshift	Field[a]	Morph.[b] Type	$\log M_\star$ ($M_\odot$)	$\log L_{0.5-8\mathrm{keV}}$ (erg s^{-1})	$S_{1.4\mathrm{GHz}}$ (μJy)	$\log L_{1.4\mathrm{GHz}}$ (erg s^{-1})	SFR ($M_\odot$ yr^{-1})
J033209.80-274442.9	0.08	4Ms CDF-S	3	9.24	39.57	45.2	27.88	0.4
J033211.54-274713.3	0.58	4Ms CDF-S	6	10.45	41.08	239.3	30.47	163.9
J033217.90-275100.1	0.12	4Ms CDF-S	4	9.90	39.52	108.9	28.58	2.1
J033220.28-275222.3	0.34	4Ms CDF-S	6	10.21	40.69	64.5	29.38	13.4
J033223.67-274938.5	0.58	4Ms CDF-S	6	10.19	40.91	41.5	29.71	28.7
J033227.73-275041.2	1.10	4Ms CDF-S	6	10.96	41.67	66.0	30.57	207.7
J033228.00-274639.7	0.25	4Ms CDF-S	3	10.22	40.01	86.3	29.19	8.6
J033229.86-274425.1	0.08	4Ms CDF-S	4	9.96	39.94	1068.0	29.17	8.3
J033230.00-274405.0	0.07	4Ms CDF-S	3	9.79	40.09	452.2	28.79	3.4
J033232.99-275030.0	0.67	4Ms CDF-S	4	10.66	41.15	38.2	29.83	37.4
J033236.19-274932.0	0.55	4Ms CDF-S	8	10.66	41.31	64.6	29.85	39.2
J033237.27-275127.5	0.69	4Ms CDF-S	6	10.11	41.23	38.9	29.87	40.9
J033238.83-274956.5	0.25	4Ms CDF-S	3	10.03	40.04	63.9	29.05	6.2
J033256.66-275316.5	0.37	E-CDF-S	8	9.56	41.39	36.3	29.20	8.9
J123559.74+621550.3	0.38	CDF-N	4	10.56	41.28	225.8	30.02	58.8
J123619.47+621252.9	0.47	CDF-N	3	10.43	41.31	65.3	29.70	27.8
J123621.09+621208.5	0.78	CDF-N	6	10.43	41.45	27.6	29.84	38.7
J123623.03+621346.7	0.48	CDF-N	8	10.07	41.39	41.8	29.53	18.7
J123634.47+621213.4	0.46	CDF-N	8	10.88	41.53	224.7	30.21	91.0
J123634.53+621241.3	1.22	CDF-N	6	10.6	42.39	201.1	31.17	813.9
J123636.86+621135.2	0.08	CDF-N	4	9.44	39.27	65.0	28.00	0.6
J123639.93+621250.4	0.85	CDF-N	4	10.6	41.87	63.3	30.29	108.8
J123643.97+621250.4	0.56	CDF-N	4	10.18	41.07	36.8	29.63	23.6
J123645.40+621901.3	0.45	CDF-N	3	10.1	41.4	41.3	29.46	15.9
J123646.60+621049.4	0.94	CDF-N	-	10.19	41.62	25.9	30.01	56.5
J123646.67+620833.6	0.97	CDF-N	3	10.89	41.93	81.7	30.54	192.0
J123648.30+621426.9	0.14	CDF-N	3	9.55	40.05	64.7	28.52	1.8
J123649.72+621313.4	0.47	CDF-N	6	9.87	41.14	59.3	29.66	25.6
J123651.12+621031.2	0.41	CDF-N	4	10.23	41.1	86.8	29.69	26.9
J123652.77+621354.7	1.36	CDF-N	-	10.48	42.15	28.8	30.43	150.6
J123652.83+621808.1	0.25	CDF-N	3	10.3	40.53	167.4	29.48	16.9
J123653.37+621140.0	1.27	CDF-N	8	10.44	42.3	84.2	30.83	374.7
J123658.34+620958.4	0.14	CDF-N	3	10.2	39.98	56.4	28.46	1.6
J123659.92+621450.3	0.76	CDF-N	8	10.38	41.45	42.1	30.00	55.5
J123700.41+621617.3	0.91	CDF-N	-	10.23	41.76	49.0	30.25	99.0
J123708.32+621056.4	0.42	CDF-N	6	10.07	41.26	66.8	29.60	21.9
J123716.82+621007.8	0.41	CDF-N	3	10.21	40.89	92.7	29.71	28.8

[a] References for redshift and fields: E-CDF-S and CDF-N galaxies are from Lehmer et al. (2008), 4Ms CDF-S galaxies are from Xue et al. (2011).
[b] Morphological Type from Bundy, Ellis, & Conselice (2005), according to the following classification: 3=Sab, 4=S, 6=Irr, 8=Merger. Sources without numerical morphological type in column 4 were classified by eye based on HST images as described in Sect.3.1 for details.

keV X-ray detection; (iii) availability of 1.4 GHz radio flux measurement for the SFR calculation or SFR determinations by Lehmer et al. (2008); (iv) the value of specific SFR (SFR/$M_\star$) larger than 10^{-10} yr^{-1}.

3.1 Selection by morphological type

We began by applying two main filtering criteria to the Lehmer et al. (2008) and Xue et al. (2011) CDF catalogs: we excluded *i*) all the AGN candidates and *ii*) objects detected only in one of the sub-bands (i.e., 0.5–2 keV and 2–8 keV), for which full band luminosity was not available. Then we proceeded with more accurate filtering, excluding the early type galaxies using the morphological classifications of galaxies in the GOODS fields (Bundy, Ellis, & Conselice 2005) and original *HST* data for those galaxies which were not included in the GOODS catalogs.

The 4 Ms CDF-S survey (Xue et al. 2011) includes 740 X-ray sources, of which 578 are classified as AGN and 162 as normal galaxies. The additional filtering mentioned above reduced the sample to 102 normal CDF-S galaxies. We cross-correlated these sources with the morphological catalog of galaxies in the GOODS South field (Bundy, Ellis, & Conselice 2005). Using a matching radius of 1.5″, we found 79 matches. Among them, we selected only sources classified as late-type or merging galaxies. The 22 sources with no match in the Bundy, Ellis, & Conselice (2005) catalog have z_{850}-band magnitude fainter than the threshold limit applied to construct the above mentioned catalog. We constructed *HST* B_{435}, V_{606}, and z_{850} color im-

age cut-outs and classified each galaxy as either early-type or late-type by visual classification. Seven sources were classified as early type galaxies and consequently were excluded from further analysis. We also excluded one source because its morphology did not allow us to clearly classify it neither as a late-type nor as an early-type galaxy. The remaining 14 sources were added to the selection of CDF-S sources obtained so far. After our morphological selection, we were left with a sample of 67 star-forming galaxies from the 4 Ms CDF-S region.

The sample from Lehmer et al. (2008) includes 225 X-ray detected late-type galaxies (selected via optical colors). Among them, 121 were classified as AGN candidates, while the remaining 104 sources were classified as normal late-type galaxies. Applying the same morphological filtering criteria as above yielded 52 sources: 37 in the CDF-N and 15 in the E-CDF-S. As Lehmer et al. (2012) point out, a single color division does not perfectly disentangle the early-type and late-type galaxy populations. In order to exclude a possible early-type galaxy contamination of the Lehmer et al. (2008) sample, we cross-matched the 52 sources with the morphological catalogs of galaxies in the GOODS North and South fields (Bundy, Ellis, & Conselice 2005). Using a matching radius of $1.5''$ we found a total of 44 matches, 11 for the E-CDF-S and 33 for the CDF-N sample. Two galaxies in the latter sample (J123603.26+621111.3 and J123627.32+621258.1) were classified as early-type and were excluded. We inspected the *HST* color image cut-outs of the four sources with no match in the GOODS-North morphological catalog. We classified three of these sources as late-type galaxies based on visual inspection. Concerning the E-CDF-S late-type galaxies from Lehmer et al. (2008), 10 of these sources were already part of the Xue et al. (2011) sample. Hereafter, we adopt the properties from the deeper 4 Ms CDF-S from Xue et al. (2011) for these galaxies. The obtained sample from Lehmer et al. (2008) consists of 35 unique star-forming galaxies.

As a check, we cross-correlated the obtained sample of CDF-N sources with the "High-SFR sample" in Paper I (Table 3). This sample was compiled by Grimm, Gilfanov, & Sunyaev (2003) and was used in Paper I as a secondary sample of unresolved star-forming galaxies in order to explore the $L_{\rm X}-$SFR relation in the high SFR regime. It includes seven galaxies from *Chandra* observations of the *Hubble Deep Field North* (HDF-N; Brandt et al. 2001) and one from the Lynx field (Stern et al. 2002). For the seven HDF-N sources, we found six counterparts. The remaining galaxy, 123716.3+621512, was not present in the GOODS catalog. We constructed the *HST* image cut-out as described above and visually classified the source as an early-type galaxy. Correspondingly, we did not consider it further in our analyses.

After this selection we were left with a sample of 104 X-ray selected star-forming galaxies drawn from the CDFs. The sample will be reduced further after the cross-correlation with radio catalogs (see Sect. 3.3).

3.2 X-ray luminosity

Both Lehmer et al. (2008) and Xue et al. (2011) provide rest-frame X-ray luminosities in the 0.5–8 keV band. In both cases the K-correction was performed assuming a power spectrum. Lehmer et al. (2008) used a photon index $\Gamma = 2$, appropriate for star-forming galaxies (e.g. Lehmer et al. 2005, and references therein), whereas Xue et al. (2011) used a photon index of $\Gamma = 1.8$, more appropriate for AGNs (e.g. Tozzi et al. 2006). For sources from the Lehmer et al. (2008) sample we used their original luminosity values. However, recomputed luminosities for galaxies from Xue et al. (2011), using their fluxes and redshifts and adopting a photon index $\Gamma = 2$.

3.3 Cross-correlation with radio catalogs and star formation rate estimates

The far-infrared (FIR) and ultraviolet (UV) luminosities are good proxies of the star formation activity in late-type galaxies. However, the use of these two estimators for CDF galaxies is limited by both the lack of rest-frame UV spectroscopic data and the sensitivity limit of the available IR observations. For these reasons, Lehmer et al. (2008) were able only to compute upper limits on SFRs for most of the sources in their galaxy sample. To measure star formation rates in the CDF galaxies, we used 1.4 GHz radio emission (e.g. Condon 1992). It has been shown (Bell 2003; Schmitt et al. 2006) that this estimator is in good agreement with both IR- and UV-based estimators used for the local resolved galaxy sample (Sect. 2). We cross-correlated the X-ray sample of star-forming galaxies produced in section 3.1 with catalogs of radio sources based on VLA observations of CDFs. For the CDF-N we used the Morrison et al. (2010) catalog, and Miller et al. (2013) catalog for the CDF-S. Using a matching radius of $1.5''$ we found a total of 39 matches with VLA sources: 23 from CDF-N and 16 from the CDF-S, of which one uniquely belongs to the selection from Lehmer et al. (2008) and 15 to the 4 Ms CDF-S sample of Xue et al. (2011). The radio flux densities $S_{1.4\,\rm GHz}$ were converted to luminosities using the following equation:

$$L_{1.4\,\rm GHz} = 4\pi d_L^2 S_{1.4\,\rm GHz}(1+z)^{\alpha-1}. \quad (1)$$

For CDF-N galaxies detected in the Morrison et al. (2010) catalog, we used the total (i.e. integrated) radio flux densities $S_{1.4\,\rm GHz}$. For CDF-N galaxies in the Miller et al. (2013) catalog, we used either peak or integrated flux densities according to their prescription. We assumed a spectral index of $\alpha = 0.8$, according to Condon (1992). The radio-based SFRs were estimated using the calibration of Bell (2003):

$$\mathrm{SFR}\,(M_\odot\,\mathrm{yr}^{-1}) = 5.55\times10^{-29} L_{1.4\,\rm GHz}(\mathrm{erg\,s}^{-1}) \quad (2)$$

3.4 X-ray sources with "missing" radio counterparts

As discussed in Section 3.3, only a fraction X-ray selected normal late-type galaxies have radio counterparts: 23 out of 35 CDF-N sources ($\sim 66\%$) and 16 out of 68 CDF-S sources ($\sim 24\%$).

In Fig. 2 we plot the 1.4 GHz flux versus 0.5–8 keV flux for the entire sample of CDF sources classified as normal late-type galaxies. For sources undetected in radio we plot upper limits. The latter were derived from the publicly-available radio RMS maps of both the GOODS-N VLA

Deep 20cm Radio Survey[2] (Morrison et al. 2010) and the VLA 1.4GHz Survey of the Extended Chandra Deep Field South: Second Data Release[3] (Miller et al. 2013). The plotted upper limits in Fig. 2 are at the 5σ level. For reference, the solid line shows our best fitting $L_{\rm X}$ − SFR relation derived in Section 4, eq. (4), converted to flux units. To calculate the solid line, the average value of redshift among CDF galaxies is assumed. It can be seen in Fig. 2 that the radio-undetected sources span both X-ray bright as well as X-ray faint sources with little variation in the radio limits. If the galaxies with the highest X-ray fluxes, at the few$\times 10^{-16}$ erg cm^{-2} s^{-1} level, followed the average L_X-SFR relation, we would have expected them to be detected in the radio band. On the other hand, some the X-ray faint sources may be normal star-forming galaxies that have remained undetected because of the insufficient sensitivity of the radio data.

In order to investigate the nature of the X-ray sources undetected in the radio band, we stacked the 0.5–2 keV and 2–8 keV data of these sources to obtain their average X-ray emission in each bandpass and infer their mean spectral slopes. The details of the data reduction and stacking procedure used are described in detail in Section 4.2 of Lehmer et al. (2008). The stacked X-ray spectrum was fitted with a power law model, giving the photon index of $\Gamma = 1.53\pm0.09$. We further divided galaxies into two groups, separated by the median X-ray flux, $f_{\rm X} \sim 10^{-16}$ erg cm^{-2} s^{-1} and obtained the mean photon indices of $\Gamma = 1.53\pm0.11$ and $\Gamma = 1.66 \pm 0.15$ for the bright and faint groups respectively. For comparison, we stacked the sample of sources detected in both X-ray and radio and obtain a mean photon index $\Gamma = 1.99 \pm 0.10$.

The radio catalogs include only $\geqslant 5\sigma$ detections. In order to probe deeper, we searched for sources on the radio maps down to 3σ and selected those within $1.5''$ from the positions of X-ray sources. We found ten sources, three in the CDF-N field and seven in the CDF-S field, one of which had not high enough specific SFR to pass our selection criterion (see Section 3.5). We measured their radio intensities as follows. For the CDF-N we performed a Gaussian fit on both the $1.7''$ and $3''$ radio maps. Primary beam correction was applied along with a correction for radial bandwidth smearing. The results for each resolution image were then compared and the best fit was selected. If the peak SNR was more than 10% higher on the lower-resolution image then that result was used (Owen & Morrison 2008). Finally, if the total flux density of the source was significantly larger at lower resolution then that result was adopted. In cases where the results appeared inconsistent, the images were examined to resolve the issue. One of the three CDF-N sources, $J123727.68+621036.3$ appears to be a possible FRI source (see e.g., Morrison et al. 2003). It is extended in radio and therefore it was not included in the original radio catalog that we cross-matched (see Section 3.3). As this sources appears to be a radio-loud AGN with twin radio jets, we excluded it from the following analysis. For the ECDF-S field only mosaicked radio images are publicly available, therefore the radial bandwidth smearing correction could not be applied. We performed a Gaussian fit using the available maps and adopted the resulting peak flux for the radio counterparts to the X-ray sources. The X-ray stacking analysis of the sources with radio counterparts in the 3-5σ range yielded an average $\Gamma = 1.30 \pm 0.17$, which is consistent with that obtained above for radio-undetected sources. We also investigated possible variations of the effective stacked photon index with the $L_{\rm X}$/SFR ratio and found no significant trend.

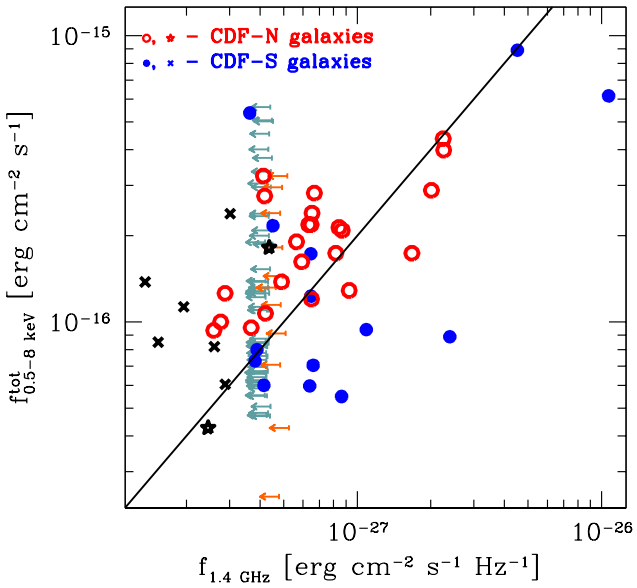

Figure 2. 1.4 GHz flux versus 0.5–8 keV flux for the whole sample of CDFs. The plot shows 39 late-type galaxies in both North (filled blue circles) and South (empty red circles) fields, that were detected in both X-ray (Lehmer et al. 2008; Xue et al. 2011) and radio (Morrison et al. 2010, Miller et al. 2013) (see Sect. 3). Black empty stars and crosses indicate sources with radio detection significance between $3\sigma <$ SNR $< 5\sigma$ in CDF-N and CDF-S respectively. These sources were not included in the radio catalogs mentioned above (Sect. 3.4). The 64 X-ray detected late-type galaxies with radio upper limits are plotted with cyan (CDF-S) and orange (CDF-N) arrows at 5σ. The solid line is our best fitting $L_{\rm X}-$SFR relation, eq. (4), converted in flux units.

Thus, galaxies detected in both X-ray and radio bands have X-ray spectra typical for star-forming galaxies (e.g. Ptak et al. 1999), confirming that their X-ray emission is indeed associated with star-formation. On the other hand, Chandra sources without radio counterparts have harder spectra, $\Gamma \approx 1.4 - 1.6$, suggesting that there is likely to be some level of low-luminosity and/or obscured AGN contamination within this population. Hereafter, we therefore exclude from the analysis of the $L_{\rm X}$–SFR relation X-ray sources undetected in the radio band. Sources with $3-5\sigma$ counterparts were also excluded.

3.5 Stellar mass and specific star formation rate

As a final check, we verified that selected CDF galaxies satisfy the selection criterion applied for the sample of resolved galaxies in Paper I – that their specific SFR exceeds SFR/$M_\star > 10^{-10}$ yr^{-1}.

This was rather straightforward for late-type galax-

[2] http://www.ifa.hawaii.edu/∼morrison/GOODSN/
[3] http://www.astro.umd.edu/∼nmiller/VLA_ECDFS.html

ies selected from Lehmer et al. (2008), for which stellar mass measurements were available. For CDF-S galaxies from Xue et al. (2011), we used the multi-wavelength optical data provided in the same catalog. To be consistent with the estimations in Lehmer et al. (2008), we calculated the stellar masses using the calibration of Bell et al. (2003). In this procedure, we made use of $(r-z)$ colors and the K-band luminosity. One CDF-S source was excluded because it did not have a $z_{850}-$band magnitude estimation. The stellar mass was therefore obtained as follows:

$$\log\left(\frac{M_\star}{M_\odot}\right) = \log\left(\frac{L_{\rm K}}{L_{\rm K,\odot}}\right) - 0.092 + 0.019\,(r-z) \quad (3)$$

In particular, we derived $L_{\rm K}/L_{\rm K,\odot}$ based on K-band AB magnitudes from the MUSYC catalog (Taylor et al. 2009), and computed $(r-z)$ colors based on AB magnitudes in R-band from the ESO 2.2 m WFI R-band catalog (Giavalisco et al. 2004), and z-band magnitudes from the GOODS-S Hubble Space Telescope (HST) catalog (Giavalisco et al. 2004).

All CDF sources satisfied the SFR$/M_\star > 1\times10^{-10}$ yr^{-1} criterion.

3.6 X-ray variability and AGN candidates in the CDF-S

As an additional criterion to filter out AGN-contaminated galaxies, we used the results from Young et al. (2012) for the 4 Ms CDF-S, to separate star-forming galaxies from AGN candidates, based on their X-ray variability. We applied same criteria as in Lehmer et al. (2012), namely: (i) X-ray variability on timescales of months to years detected with the confidence of $P_{\chi^2} \gtrsim 95\%$; (ii) the 0.5–8 keV luminosity greater than $10^{41}\,{\rm erg\,s^{-1}}$ (see Young et al. 2012, for details). By cross-matching our CDF-S sources with this catalog, we found that two sources, $J033206.42-274728.7$ and $J033218.04-274718.8$, are likely to be AGNs. These sources were excluded from the analysis.

3.7 The final CDF sample

The final CDF sample consists of 39 X-ray selected galaxies with radio SFR measurements from the CDFs: 23 objects from CDF-N and 14 from CDF-S. They are listed in Table 2, along with their parameters.

The entire sample, including 21 local (resolved) galaxies, 8 LIRGs and ULIRGs and 37 CDF galaxies (66 galaxies in total) is shown in the SFR–$M_\star$ plane in Fig.1.

4 $L_{\rm X}-$SFR RELATION FOR TOTAL LUMINOSITY

We approximate the $L_{\rm X}^{\rm tot}-$SFR data (in Fig.3) with the log-linear model $\log L_{\rm X}^{\rm tot} = \log K + \beta \log {\rm SFR}$. This model was applied to local sample and CDF sample separately. Both slope β and normalization K were set as free parameters of the fit. To fit the data we used least square minimization. The results are given in Table 3, which demonstrates that the best fit parameters for the local and CDF samples are compatible. We therefore performed the joint fit to the whole

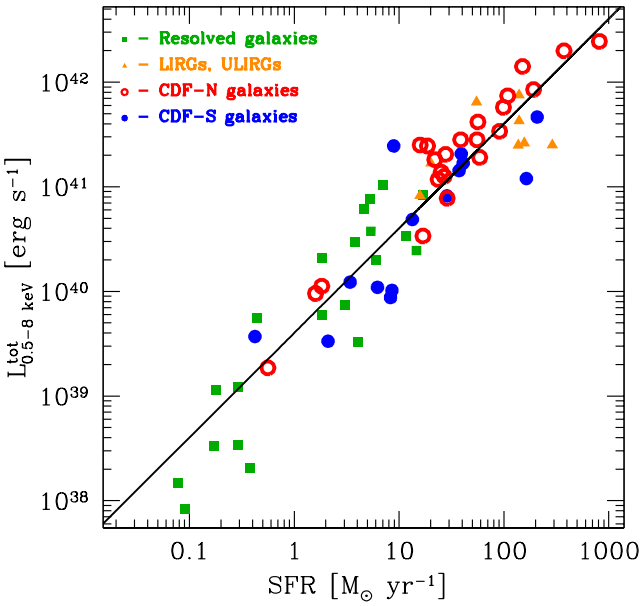

Figure 3. The $L_{\rm X}^{\rm tot}-$SFR relation. The (green) squares indicate galaxies from the local ($z=0$) resolved sample, the (orange) triangles are LIRGs and ULIRGs from the unresolved sample, described in Sect. 2 and presented in Table 1. The filled (blue) circles are late-type galaxies from the CDF-S and the and empty (red) circles are late-type galaxies from the CDF-N, selected as described in Sect. 3 and presented in Table 2. The solid line shows the linear scaling relation, obtained using the whole sample of 54 galaxies and given by eq. (4).

sample of star-forming galaxies that includes both local and CDF sources, using same model. We obtained a slope $\beta = 1.00\pm0.05$, suggesting a linear relation. The linear scaling relation obtained by fixing the slope to unity is shown in Fig. 3 and it is given by the following equation:

$$L^{\rm tot}_{0.5-8\,\rm keV}({\rm erg\,s^{-1}}) \approx (4.0\pm0.4)\times10^{39}\,{\rm SFR}\,(M_\odot\,{\rm yr^{-1}}) \quad (4)$$

where the uncertainty was computed from the scatter of the points around the best fit. The results of all fits are summarized in Table 3.

In Paper I we obtained the $L_X - SFR$ relation for X-ray point sources in star-forming galaxies $\approx 2.6\times10^{39}$ $({\rm erg\,s^{-1}})/(M_\odot\,{\rm yr^{-1}})$. Comparing the scale factor for compact sources with that in eq.(4) above we conclude that the unresolved emission contributes, on average, $\sim 1/3$ of the total 0.5–8 keV luminosity of star-forming galaxies generated per unit of SFR. This result is consistent with the preliminary estimate obtained in Paper I based on the comparison of the $L_{\rm X}-$SFR relations of the HMXBs in the resolved galaxies and total emission from unresolved galaxies. It is also consistent with the scaling relation for the ISM emission obtained in Paper II.

In the conclusion of this section we note that the result of the fitting of the $L_{\rm X}-$SFR relation depends on whether the fit was performed in the logarithmic or linear space. In the linear case, it also depends on whether the least square fit in the form $L_{\rm X} = A\times{\rm SFR}$ was performed or individual $L_{\rm X}/{\rm SFR}$ ratios were averaged (note that in the log case it is same). Note also that large scatter of points, much bigger than statistical uncertainties, ren-

ders the χ^2 minimization less appropriate. Doing the least square fit to the linear quantities, we obtain the scale of $L_{\rm X}/{\rm SFR} \approx (2.7\pm0.2)\times10^{39}$ $({\rm erg\,s^{-1}})/(M_\odot\,{\rm yr^{-1}})$. Averaging the $L_{\rm X}/{\rm SFR}$ ratio in the linear space, we obtain yet another number: $L_{\rm X}/{\rm SFR} \approx (5.4 \pm 0.6) \times 10^{39}$ $({\rm erg\,s^{-1}})/(M_\odot\,{\rm yr^{-1}})$, i.e. notably larger than in eq.(4). The value obtained in the logarithmic fit is smaller, because it gives equal weights to the low and high points.[4] As this seems to be a more correct approach and in order to be consistent with Paper I, we used the fit in the log space as default.

4.1 CDF-S vs CDF-N

Visual inspection of Fig. 3 suggests that there may be an offset in $L_{\rm X}/{\rm SFR}$ ratio between the CDF-S and CDF-N fields. To asses its statistical significance, we fitted the data for the CDF-S and CDF-N separately; the results are presented in Table 3. For the linear model, we found that the $L_{\rm X}/{\rm SFR}$ ratios for CDF-N and CDF-S differ by 0.27 dex. The statistical significance of this difference measured with respect to the dispersion of the points is $\approx 2.2\sigma$, i.e. the offset is marginally significant. We also note that the CDF-N galaxies appear to have smaller scatter, ≈ 0.2 dex vs ≈ 0.4 dex.

To explore the origin of the difference between the fields, we first investigate importance of the Eddington bias in our CDF samples. To this end, we compared the fluxes of CDF-N and CDF-S sources with the sensitivity limits, in the 0.5–8 keV band, of the respective fields, 7.1×10^{-17} erg cm^{-2} s^{-1} for the CDF-N (Alexander et al. 2003) and 3.2×10^{-17} erg cm^{-2} s^{-1} for the CDF-N (Xue et al. 2011). We selected only CDF galaxies with flux above three times the sensitivity limit of the given field. Such a selection shrank the sample by ∼50%. For the new sample we repeated the fitting procedure and obtained $\log K = 39.56\pm0.15$ for CDF-S and $\log K = 39.59\pm0.08$ for CDF-N. These numbers are in perfect agreement with each other as well as with the local sample (Table 3) and, taken at the face value, may suggest that the offset between CDF-S and CDF-N is caused by the Eddington bias. We note however, that whereas for the CDF-N the $\log K$ shifts downwards for the reduced sample, as it should be expected if X-ray fluxes were affected by the Eddington bias, CDF-S data shows the opposite behavior, with the best fit $\log K$ increasing for the reduced sample. Thus, change of the $\log K$ in CDF-S and good agreement between the two fields in the reduced sample was a result of statistical fluctuations. We conclude that although the Eddington bias may explain a part of the offset between CDF-S and CDF-N, it is unlikely that it is responsible for all of it.

We can exclude that systematic differences in Chandra calibration of the CDF-N and CDF-S would affect the observed $L_{\rm X}/{\rm SFR}$ offset. Indeed, the 1 Ms CDF-S and 2 Ms CDF-N were analyzed in exactly the same way by Alexander et al. (2003). The data for both surveys were taken throughout the first three years of the mission, therefore comparing the 1 Ms CDF-S with 4 Ms CDF-S systematics would provide us with an approximation of the difference in calibration between the CDF-N and CDF-S. In particular, sources with flux $F_{0.5-8\,{\rm keV}} > 10^{-15}$ erg cm^{-2} s^{-1} have mean $F_{0.5-8\,{\rm keV}}(4\,{\rm Ms})/{\rm F}_{0.5-8\,{\rm keV}}(1\,{\rm Ms}) = 0.994$, i.e. a difference of ∼ 0.5%, which is negligible for the aims of the present work. Furthermore, the amplitude of the difference $\Delta\log(K) \approx 0.27$ dex, corresponds to the factor of ≈ 1.9 difference in flux calibration, which is far beyond the calibration uncertainties expected for Chandra.

Another potential source of systematic difference in the L_X/SFR between the two fields is offset in the radio data. This however requires a special investigation which is beyond the scope of this paper.

4.2 Comparison with previous results

Ranalli, Comastri, & Setti (2003) studied the $L_{\rm X} - {\rm SFR}$ relation using X-ray data from ASCA and BeppoSAX satellites. In Paper I, we converted their X-ray luminosity and SFR to make them consistent with the analogous quantities used here and derived: $L_{0.5-8\,{\rm keV}} \approx 1.6 \cdot 10^{39} \times {\rm SFR}$, i.e. more than ∼ 2 times smaller than our eq.(4). The rather large discrepancy is likely caused by the confusion in the definition of SFR proxies (see detailed discussion in Paper I). On the other hand, the $L_{\rm X} - L_{\rm IR}$ relation of Ranalli, Comastri, & Setti (2003), transformed to be compatible with our definitions is $L_{0.5-8\,{\rm keV}} \approx 2.4 \cdot 10^{-4} \times L_{\rm IR}$. The scale in this relation is ≈ 27% larger that the scale in the corresponding relation for HMXBs from Paper I (eq.(23)), consistent with ∼ 1/4 contribution of hot ISM and other unresolved emission components to the total luminosity – see the discussion after eq.(4) above. This proves that the underlying $L_{\rm X} - L_{\rm IR}$ relations are fully compatible and the discrepancy in the $L_{\rm X} - {\rm SFR}$ relation is due the difference in the use and definitions of SFR proxies.

Persic & Rephaeli (2007) investigated the relation between the total X-ray emission from normal and starburst (ULIRGs) galaxies in the 2–10 keV band and the SFR derived from infrared luminosity. Using their eq. (10) and converting the 2–10 keV luminosity to the 0.5–8 keV band (a factor of 1.28) we obtain: $L_{0.5-8\,{\rm keV}} \approx 4.9 \cdot 10^{39} \times {\rm SFR}$. This relation is consistent, within a factor of ∼ 1.4 with our eq. (4). On the other hand, in Paper I we found a rather large disagreement between our $L_{\rm X} - {\rm SFR}$ relations for the HMXB luminosity.

Lehmer et al. (2010) recently studied the relation between 2–8 keV luminosity and SFR for a sample of nearby LIRGs using *Chandra* observations. They obtained the hard band luminosities by modeling the X-ray spectra in 0.5–8 keV band using Galactic absorption, a thermal component and a power-law component. This is consistent with the model we used to fit the X-ray spectra of our sample of LIRGs and ULIRGs and determine their X-ray luminosities. In order to compare our results with the $L_{\rm X} - {\rm SFR}$ relation obtained by Lehmer et al. (2010), we converted their 2–8 keV luminosity to the 0.5–8 keV band. We assumed same model as above, with average quantities from our ULIRGs spectral fits ($\Gamma \sim 1.7$, $kT \sim 0.6$ keV, $N_{\rm H} \sim 2 \times 10^{21}$ cm^{-2} and thermal-to-power-law normalization ratio of ∼ 0.5). For the linear (first line in their Table 4) $L_{\rm X} - {\rm SFR}$ relation in Lehmer et al. (2010) we obtain a scale factor $L_{\rm X}/{\rm SFR} \approx 2.9 \times 10^{39}$ $({\rm erg\,s^{-1}})/(M_\odot\,{\rm yr^{-1}})$. This result is also in a reasonable agreement with our eq. (4).

[4] Indeed, for two measurements yielding $y_1 = a$ and $y_2 = 10\,a$ the logarithmic (geometrical) average is $\langle y\rangle_{log} \approx 3.16\,a$ while the linear average is $\langle y\rangle_{lin} = 5.5\,a$, i.e. is nearly twice larger.

Table 3. Summary of the parameters for $L_{\rm X}-{\rm SFR}$ relations obtained from least-squares fit.

	FREE SLOPE			LINEAR FIT	
Sample	$\log K$	β	σ (dex)	$\log K$	σ (dex)
$z=0$ galaxies	39.53 ± 0.09	1.04 ± 0.08	0.42	39.56 ± 0.08	0.42
CDF galaxies	39.66 ± 0.12	0.98 ± 0.07	0.33	39.64 ± 0.05	0.32
CDF-S galaxies	39.65 ± 0.21	0.85 ± 0.16	0.41	39.47 ± 0.11	0.41
CDF-N galaxies	39.76 ± 0.11	0.98 ± 0.06	0.22	39.74 ± 0.05	0.21
all	39.57 ± 0.07	1.03 ± 0.05	0.37	39.60 ± 0.05	0.37

Note. The parameters are relative to the least-squares fit to the data with the relation $\log L_{\rm X} = \log K + \beta \log {\rm SFR}$, respectively setting the slope β free and fixing it to unity. σ is the dispersion around the best-fitting relation. See Sect. 2.2 and 3.2 for the definition of the X-ray luminosities, Sect. 6 of Paper I and 3.3 of present work for the definition of SFR for $z=0$ sample and CDF galaxies respectively.

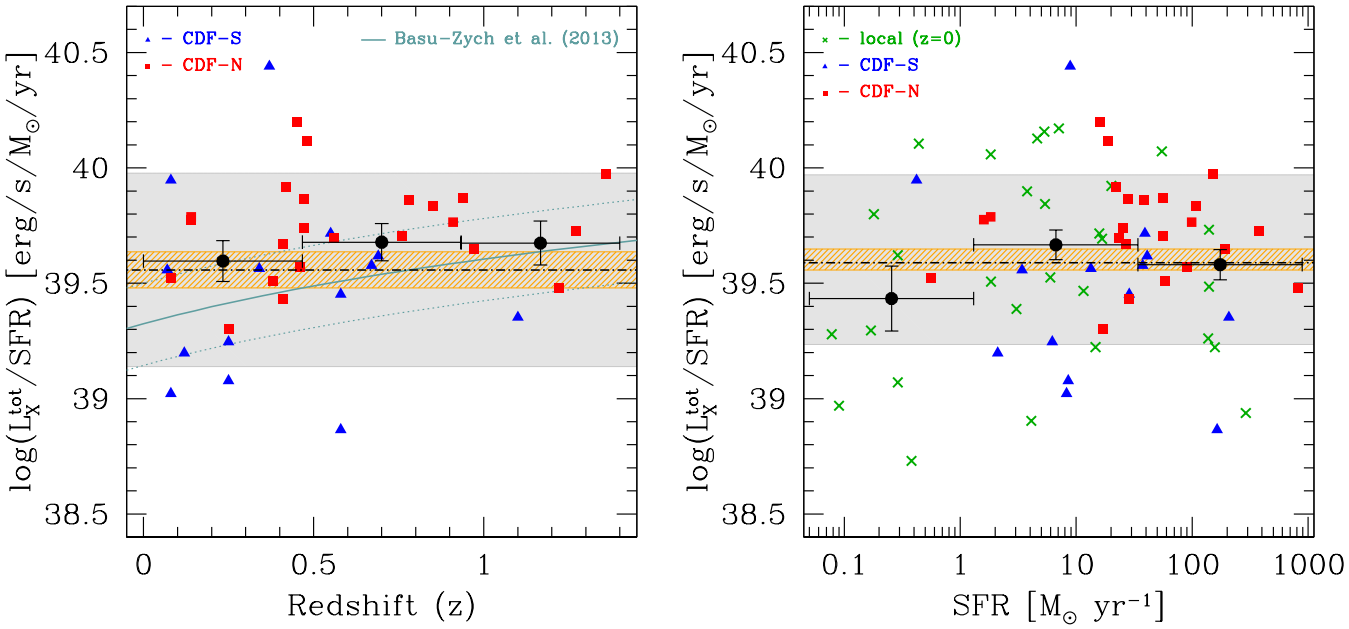

Figure 4. Dependence of the $L_{\rm X}^{\rm tot}-{\rm SFR}$ relation on redshift (left panel) and star formation rate (right panel).The symbols without error bar indicate individual galaxies. The (black) filled circles with error bars show their average values within each redshift (left) or SFR (right) bin. The vertical error bars are uncertainties of the average values computed from the *rms* of points in the given bin. In the left panel, the horizontal dot-dashed line shows the average local $L_{\rm X}^{\rm tot}$/SFR ratio. Its uncertainty is shown by the narrower (orange) shaded area, while the wider (grey) shaded area shows the *rms* of the points. On the right hand panel, the horizontal line and the shaded areas show similar quantities computed using all galaxies. For comparison, in the left-hand panel we plot the best-fit model from Basu-Zych et al. (2013) stacking results that is appropriate for the median SFR (solid, grey curve) and interquartile SFR range (dotted, grey curves) of our CDF galaxy sample.

5 CONSTRAINTS ON THE REDSHIFT AND SFR DEPENDENCE OF THE $L_{\rm X}-{\rm SFR}$ RELATION

The composition of the sample (29 galaxies at the redshift $z=0$ and 25 galaxies at $z\approx0.1-1.3$) allows us to constrain a possible redshift evolution of the X-ray emission produced per unit SFR. To this end, we grouped the CDF galaxies into three redshift bins of equal width spanning from $z=0$ to $z=1.3$ and computed the average $L_{\rm X}^{\rm tot}$/SFR ratio and its uncertainty within each bin. Same quantities were computed for the local sample of galaxies, to characterize the $z=0$ population. The result of this calculation is shown in Fig. 4. It is evident from the figure, that the average values for CDF galaxies are consistent, within uncertainties, between each other and with the average quantity for local galaxies. To confirm this, we applied the Spearman's rank test and we found no statistically significant correlations, neither for the individual values nor for the average points, with the

corresponding probabilities of $P \sim 27\%$ and $P \sim 20\%$ respectively.

Thus, the total X-ray emission produced per unit SFR by late-type galaxies does not show statistically significant trends with the redshift up to $z \sim 1.3$. The sensitivity of this analysis is sufficient to rule-out evolution larger than $\sim 0.1-0.2$ dex (by factor of $\sim 1.3-1.6$) between $z \sim 0$ and $z \sim 1.3$, although as a caveat we should note that the high redshift bin contained only 4 galaxies. This conclusion is in agreement with results of the X-ray stacking analysis of late-type galaxies (Lehmer et al. 2008) and with calculations of the maximal contribution of star-forming galaxies to the unresolved CXB intensity (Dijkstra et al. 2012).

Recent population synthesis calculations by Fragos et al. (2012) predict that the ratio of the 0.5–8 keV luminosity to the SFR increases by a factor of $\sim 1.3-1.4$ between redshift $z = 0$ and $z \sim 1.3$. Such an evolution is within the uncertainties of our results.

Furthermore, recent deep X-ray stacking of the 4 Ms CDF-S data, Basu-Zych et al. (2013) suggested that there may be mild evolution of the rest-frame 2–10 keV luminosity per unit SFR with the redshift and SFR. In Figure 4, we show the expected redshift evolution of $L_{\rm X}$/SFR as a function of redshift, from Basu-Zych et al. (2013), for SFRs equal to the median SFR (*solid grey curve*) and interquartile SFR range (*dotted grey curve*) of our CDF galaxy sample. These curves have been corrected to our choice of X-ray bandpass and IMF. It is obvious from Figure 4 that although our data does not require redshift evolution of the scale in the mean $L_{\rm X}$/SFR relation, it is also consistent with the mild evolution found by Basu-Zych et al. (2013).

Finally, in the right hand panel of Fig.4 we constrain the possible dependence of the $L_{\rm X}$/SFR ratio on the SFR. Using both local and CDF galaxies, we bin the data into 3 SFR bins and compute the average and its uncertainty (*rms*-based) for each redshift bin. The formal $\chi^2 = 4.8$ for the binned data, with 2 degrees of freedom. The probability of having such (or bigger) value of the χ^2 is $\sim 9\%$, which is equivalent to $\sim 1.5\,\sigma$ detection. This may or may not indicate the existence of some SFR dependence in the $L_{\rm X}-$SFR ratio. If any, the amplitude of this dependence also does not exceed ~ 0.15 dex (a factor of ~ 1.4). Finally, we note that due to the observer's bias (see Sect. 2.3 of Paper I), the effect of statistics of the small numbers (Gilfanov, Grimm, & Sunyaev 2004) is not strong in our sample.

6 SUMMARY

Based on the sample of nearby resolved galaxies more distant ULIRGs at intermediate distances and star-forming galaxies from the CDFs, we construct a sample of 54 star-forming galaxies spanning the range of redshifts from $z = 0$ up to $z = 1.3$ and the range of star formation rates SFR $\sim 0.1-10^3$ $M_\odot$/yr (Fig.1). Using this sample, we calibrate the $L_{\rm X}-$SFR relation for the 0.5–8 keV band luminosity (Fig.3). We find that $L_{\rm X}-$SFR dependences for the local and CDF samples are consistent with linear relations with the typical accuracy of ~ 0.1 in the slope. The linear $L_{\rm X}-$SFR relation obtained for the entire sample is given by eq.(4). We did not find any statistically significant trends in the scaling relation with the redshift and star formation rate with the upper limit on the possible variations in the $L_{\rm X}$/SFR ratio of $\sim 0.1-0.2$ dex (a factor of $\sim 1.3-2.6$) (Fig.4). This property makes the X-ray emission a powerful tool to measure star formation rate in a broad range of redshifts and star formation regimes, which can be applied *en masse* to faint distant galaxies.

ACKNOWLEDGMENTS

SM gratefully acknowledges financial support through the NASA grant AR1-12008X and funding from the STFC grant 664 ST/K000861/1.The authors are grateful to Ken Kellermann for providing them with both radio RMS map and the source list of the second data release of the VLA 1.4 GHz Survey of the Extended *Chandra* Deep Field South, prior to publication. The authors thank William Forman for his valuable comments and suggestions to improve the quality of the paper. This research made use of *Chandra* archival data and software provided by the *Chandra* X-ray Center (CXC) in the application package CIAO. This research has made use of SAOImage DS9, developed by Smithsonian Astrophysical Observatory. The *Spitzer Space Telescope* is operated by the Jet Propulsion Laboratory, California Institute of Technology, under contract with the NASA. *GALEX* is a NASA Small Explorer, launched in 2003 April. This publication makes use of data products from Two Micron All Sky Survey, which is a joint project of the University of Massachusetts and the Infrared Processing and Analysis Center/California Institute of Technology, funded by the NASA and the National Science Foundation. This research has made use of the NASA/IPAC Extragalactic Database (NED) which is operated by the Jet Propulsion Laboratory, California Institute of Technology, under contract with the National Aeronautics and Space Administration.

REFERENCES

Alexander, D. M., Bauer, F. E., Brandt, W. N., et al. 2003, AJ, 126, 539
Barger A. J., et al., 2003, AJ, 126, 632
Basu-Zych, A. R., Lehmer, B. D., Hornschemeier, A. E., et al. 2013, ApJ, 762, 45
Bell E. F., 2003, ApJ, 586, 794
Bell E. F., McIntosh D. H., Katz N., Weinberg M. D., 2003, ApJS, 149, 289
Brandt W. N., et al., 2001, AJ, 122, 2810
Bundy K., Ellis R. S., Conselice C. J., 2005, ApJ, 625, 621
Condon J. J., 1992, ARA&A, 30, 575
Cowie L. L., Barger A. J., Hasinger G., 2012, ApJ, 748, 50
Dijkstra M., Gilfanov M., Loeb A., Sunyaev R., 2012, MNRAS, 421, 213
Drozdovsky I. O., Karachentsev I. D., 2000, A&AS, 142, 425
Drozdovsky I. O., Schulte-Ladbeck R. E., Hopp U., Greggio L., Crone M. M., 2002, AJ, 124, 811
Fragos T., et al., 2012, arXiv, arXiv:1206.2395, submitted to ApJ
Giavalisco M., et al., 2004, ApJ, 600, L93
Gilfanov M., Grimm H.-J., Sunyaev R., 2004, MNRAS, 351, 1365

Gilli R., et al., 2003, ApJ, 592, 721
Grimes J. P., Heckman T., Strickland D., Ptak A., 2005, ApJ, 628, 187
Grimm H.-J., Gilfanov M., Sunyaev R., 2003, MNRAS, 339, 793
Grisé F., Pakull M. W., Soria R., Motch C., Smith I. A., Ryder S. D., Böttcher M., 2008, A&A, 486, 151
Ismail H. A., Alawy A. E., Takey A. S., Issa I. A., Selim H. H., 2005, JKAS, 38, 7
Kellermann K. I., Fomalont E. B., Mainieri V., Padovani P., Rosati P., Shaver P., Tozzi P., Miller N., 2008, ApJS, 179, 71
Li J.-T., Wang Q. D., 2012, arXiv, arXiv:1210.2997
Lehmer B. D., et al., 2005a, AJ, 129, 1
Lehmer, B. D., Brandt, W. N., Alexander, D. M., et al. 2005b, ApJS, 161, 21
Lehmer B. D., et al., 2008, ApJ, 681, 1163
Lehmer B. D., Alexander D. M., Bauer F. E., Brandt W. N., Goulding A. D., Jenkins L. P., Ptak A., Roberts T. P., 2010, ApJ, 724, 559
Lehmer B. D., et al., 2012, ApJ, 752, 46
Luo B., et al., 2008, ApJS, 179, 19
Makarova L. N., Karachentsev I. D., 2003, Ap, 46, 144
Mineo S., Gilfanov M., Sunyaev R., 2011, AN, 332, 349
Mineo S., Gilfanov M., Sunyaev R., 2012a, MNRAS, 419, 2095 (Paper I)
Mineo S., Gilfanov M., Sunyaev R., 2012b, MNRAS, 426, 1870 (Paper II)
Miller, N. A., Bonzini, M., Fomalont, E. B., et al. 2013, arXiv:1301.7004
Morrison G. E., Owen F. N., Ledlow M. J., Keel W. C., Hill J. M., Voges W., Herter T., 2003, ApJS, 146, 267
Morrison G. E., Owen F. N., Dickinson M., Ivison R. J., Ibar E., 2010, ApJS, 188, 178
Owen F. N., Morrison G. E., 2008, AJ, 136, 1889
Persic M., Rephaeli Y., 2007, A&A, 463, 481
Ptak, A., Serlemitsos, P., Yaqoob, T., & Mushotzky, R. 1999, ApJS, 120, 179
Ranalli P., Comastri A., Setti G., 2003, A&A, 399, 39
Saha A., Thim F., Tammann G. A., Reindl B., Sandage A., 2006, ApJS, 165, 108
Sanders D. B., Mazzarella J. M., Kim D.-C., Surace J. A., Soifer B. T., 2003, AJ, 126, 1607
Sakai S., Madore B. F., 1999, ApJ, 526, 599
Saviane I., Hibbard J. E., Rich R. M., 2004, AJ, 127, 660
Schmitt H. R., Calzetti D., Armus L., Giavalisco M., Heckman T. M., Kennicutt R. C., Jr., Leitherer C., Meurer G. R., 2006, ApJ, 643, 173
Stern D., et al., 2002, AJ, 123, 2223
Taylor E. N., et al., 2009, ApJS, 183, 295
Tozzi P., et al., 2006, A&A, 451, 457
Tully R. B., 1988, Sci, 242, 310
Tully R. B., Rizzi L., Shaya E. J., Courtois H. M., Makarov D. I., Jacobs B. A., 2009, AJ, 138, 323
Willick J. A., Courteau S., Faber S. M., Burstein D., Dekel A., Strauss M. A., 1997, ApJS, 109, 333
Xue Y. Q., et al., 2011, ApJS, 195, 10
Young M., et al., 2012, ApJ, 748, 124

This paper has been typeset from a TEX/ LATEX file prepared by the author.